SAND2015-2423C
ILASS Americas 27th Annual Conference on Liquid Atomization and Spray Systems, Raleigh, NC, May 2015

Demonstration of High Speed (20 kHz) Digital Inline Holographic (DIH) Imaging of a Multiphase Event: Drop Impact on a Thin Liquid Film

Daniel R. Guildenbecher[*,a], and Paul E. Sojka[b]
[a]Sandia National Laboratories, Albuquerque, NM, USA
[b]School of Mechanical Engineering, Purdue University, West Lafayette, IN, USA

Abstract

Digital in-line holography (DIH) is a laser based measurement technique that provides 3D quantification of a particle field, such as a spray. Most previous applications of DIH are limited to low-speed (10s of Hz or less) recording rates. In this work, we demonstrate what is believed to be one of the first applications of high speed DIH (20 kHz, 1024 × 1024 pixels) to a transient spray process. Analysis of the impact of a water drop on a thin film of water reveals that kHz DIH results in higher positional uncertainty compared to previous results using low-speed CCDs. However, the temporal resolution allows measured positions to be fit to smooth trajectories over a large number of frames. Consequently, for this application, kHz DIH produces overall 3D positional accuracy exceeding previous low speed DIH results with the added benefit of temporal resolution. Here, the technique is applied to study four impact Weber numbers ranging from 381 to 1160. Non-dimensional fragment diameters are shown to increase as a function of non-dimensional time, while the non-dimensional velocities decrease over time. The improved resolution of the temporal statistics provided here is expected to be beneficial for future model development and validation.

[*]Corresponding author: drguild@sandia.gov

Introduction

Digital in-line holography (DIH) is an optical technique in which a collimated laser beam illuminates an object field. The resulting diffraction pattern is digitally recorded, and numerical reconstruction of the volumetric field is performed via solution of the diffraction integral equations [1, 2]. DIH has a number of advantages for quantification of multiphase, particle flows including: (1) individual particles can be located in three-dimensional (3D) space; (2) the size and shape of each particle can be measured at their in-focus location; (3) 3D particle velocities can be determined from two or more holograms recorded with short interframe times; (4) non-spherical particles can be quantified; and (5) knowledge of the index of refraction is not necessarily required. Due to these advantages, DIH has been explored for applications to flows of gaseous particulates [3, 4], liquid drops [5-7], and solid particulates [8-10], among many others.

For accurate recording and reconstruction of digital holograms, ideal sensors have large pixel counts, small pixel pitch, and low noise. Large format CCD sensors, of the type typically employed in Particle Image Velocimetry (PIV), are commonly used. However, such sensors are low speed, with maximum record rates of 10s of Hz. While double pulsed lasers can be used to achieve short interframe times between pairs of images, these sensors are nevertheless insufficient to capture the vast majority of transient dynamics of interest to the multiphase science community.

High-speed, digital imaging has been rapidly advancing, and many scientific labs now have CMOS cameras capable of recording ~ 1 megapixel images at rates of 10s of kHz. Combined with DIH, this technology would allow for quantification of transient, 3D particulate flows. Yet, the literature contains limited examples of high-speed DIH [11, 12]. This is likely due to real and perceived challenges arising from higher noise characteristics, smaller pixel counts, and larger pixel sizes of kHz CMOS cameras compared to low-speed CCDs. In addition, large data sets require new processing techniques which can accurately and efficiently quantify particle dynamics from gigabytes of raw data.

Here we present our efforts to explore high-speed kHz DIH and propose new methods to overcome the aforementioned challenges. To demonstrate the technology, the fragments which result from the impact of a single drop on a thin film are investigated. Previously we investigated this flow with low-speed DIH [13], and those results are used as a baseline for comparison with kHz data presented here.

The impact of single drops on thin films has been widely studied for applications to fuel sprays in combustion engines with reviews provided by Yarin [14] and Moreira et al. [15]. For liquids of low viscosity, the most relevant non-dimensional parameters are the impact Weber number, $We = \rho d_0 v_0^2/\sigma$, the non-dimensional time, $\tau = (t\text{-}t_0)v_0/d_0$, and non-dimensional film thickness, $\delta = h/d_0$. Here, ρ is the liquid density, d_0 is the initial spherical diameter, v_0 is the impact velocity, σ is the interfacial surface tension, t_0 is the impact time, and h is the film thickness. Figure 1 shows typical backlit high-speed images recorded at the conditions studies here. A crown forms shortly after impact. Instabilities on the crown rim lead to the formation of fingers, which further breakup to form fragments. As the *We* increases, the speed and number of fragments also increases.

Experimental configuration

The experimental configuration for kHz DIH is illustrated in Figure 2. As was previously done in [13], liquid drops are produced from deionized water ($\rho = 1000$ kg/m^3 and $\sigma = 0.072$ N/m assumed) using a droplet generator consisting of a syringe pump (KD Scientific model KDS100) and syringe tip (Nordson EFD, 20 gauge dispensing tip). Individual drops leave the syringe tip with approximately zero velocity and are accelerated due to gravity before impacting the center of a thin film also made of deionized water. The film is held inside a rubber o-ring with square cross-section affixed to a smooth acrylic surface. The images in Figure 1 indicate that the thickness of the film is equal to that of the o-ring ($h = 2.35$ mm), and the extent of the film (50.8 mm diameter) is sufficiently large to prevent interaction of its edges with the breakup process. Finally, the drop production rate is sufficiently slow (on the order of 1/8 Hz) such that the conditions considered here can be assumed equivalent to the impact of an individual drop on an infinite, initially quiescent thin film.

The illumination source is a Coherent Lasers Verdi G6 CW-laser producing up to 6 W at 532 nm. The output beam is polarized, spatially filtered, and then telescopically expanded (Thorlabs BE15M-A) from ~3 to ~48 mm in diameter. After the beam passes through the particle field, the resulting diffraction images are recorded at 20 kHz with 1024 × 1024 resolution using a Photron SAZ monochrome camera (20 μm pixel pitch, 12 bit ADC depth). To ensure the particles do not move significantly during the exposure, the minimum possible integration time of 250 ns is utilized.

In our previous work [13], DIH images were recorded on a bare CCD (without front objective). While such a configuration could be utilized here, it would require placement of the high-speed camera within close proximity of the drops. Rather, to protect the camera sensor and provide some ability to alter the magnification, we choose to use a lens (Infinity K2/Distamax long distance microscope with CF1 objective) to relay the holographic image from the front fo-

cal-plane to the sensor. To spatially calibrate the magnified image, a glass slide containing dots with known spacing (Max Levy Autograph distortion target DA020) is placed within the DIH line-of-sight and traversed in the z direction until it is in focus at the front focal plane. Analysis of this calibration image is used to quantify the magnification and effective pixel size. Here a magnification of between 1.26 and 1.03 is found with an effective pixel size between 15.8 and 19.4 μm. Variations in the magnification are a result of realigning the setup during the experimental campaign.

In addition, a second high-speed camera is used to record backlit images of the breakup process at 20 kHz. This camera is oriented orthogonal to the DIH field of view (not shown in Figure 2) and is synchronized to the DIH camera such that individual frames are recorded at the same instant in both cameras. Figure 1 gives example results.

Finally, the impact velocity is adjusted by altering the height of the syringe tip with respect to the film (between ~600 and ~2250 mm). The recording process is initiated when a drop falls through a laser beam, thereby interrupting the signal to a photodiode. The changing photodiode signal triggers the DIH and second cameras' operation. A Stanford Research delay unit (DG535) is used to synchronize the cameras' start times.

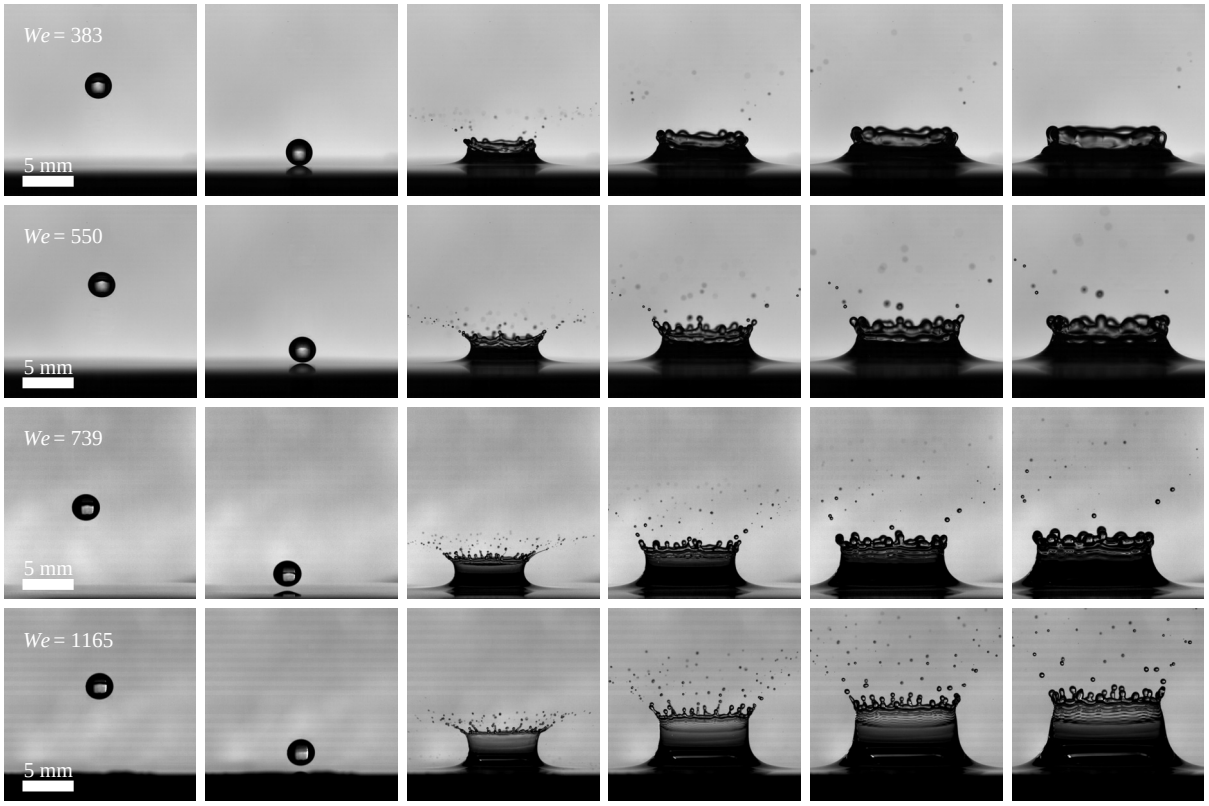

Figure 1. Select results from high-speed backlit imaging.

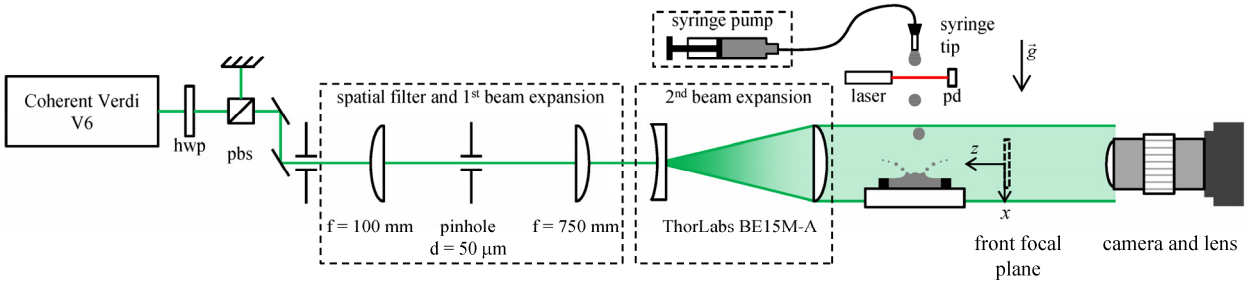

Figure 2. Experimental configuration for kHz DIH of drop impact on a thin film. *hwp*: half wave plant, *pbs*: polarizing beam splitter, *pd*: photodiode.

DIH Processing

The top row of Figure 3 shows example holograms. These images are numerically refocused by solving the diffraction integral equation,

$$E(x,y;z) = \left[I_0(x,y) E_r^*(x,y) \right] \otimes g(x,y;z), \quad (1)$$

where E is the reconstructed complex amplitude at optical depth, z; I_0 is the recorded hologram; x, y, are the spatial coordinates in the hologram plane (see Figure 2 for coordinate system); E_r^* is the conjugate reference wave (assumed constant for a plane wave); $\otimes$ is the convolution operation; and g is the diffraction kernel [1, 2]. Equation (1) is numerically evaluated to find $E(x,y;z)$ at any z, and the reconstructed light field is visualized using its amplitude, $A = |E|$. For example, the second row in Figure 3 shows the reconstructed amplitude when the hologram images in the top row are numerically refocused to the z-location of impact (z_0 = 105.9 mm). In-focus features of the crown and fragments are observed. In addition, out-of-focus twin images, which appear as rings around the in-focus features [1, 2], are also observed.

Similar to our previous work [13], the hybrid method described in [16-18] is applied to each hologram frame in order to extract the fragment x, y, z-positions and in-plane (x-y) morphologies. In this case, Eq. (1) is applied to sweep through 2001 z-positions with an interplane spacing of 40 μm. From this, a minimum amplitude and maximum edge sharpness map is calculated. Next, a global optimal threshold [18] is used to derive an initial estimate of in-plane fragment sizes and locations. Following this, a first hybrid refinement [17] is applied to determine fragment z-locations based on the z-locations of maximum edge sharpness. Finally, the in-plane morphologies are refined by a second hybrid refinement [17] performed at the measured z-location of each fragment. To minimize detection of false particles, no region is accepted with $d \leq 40$ μm.

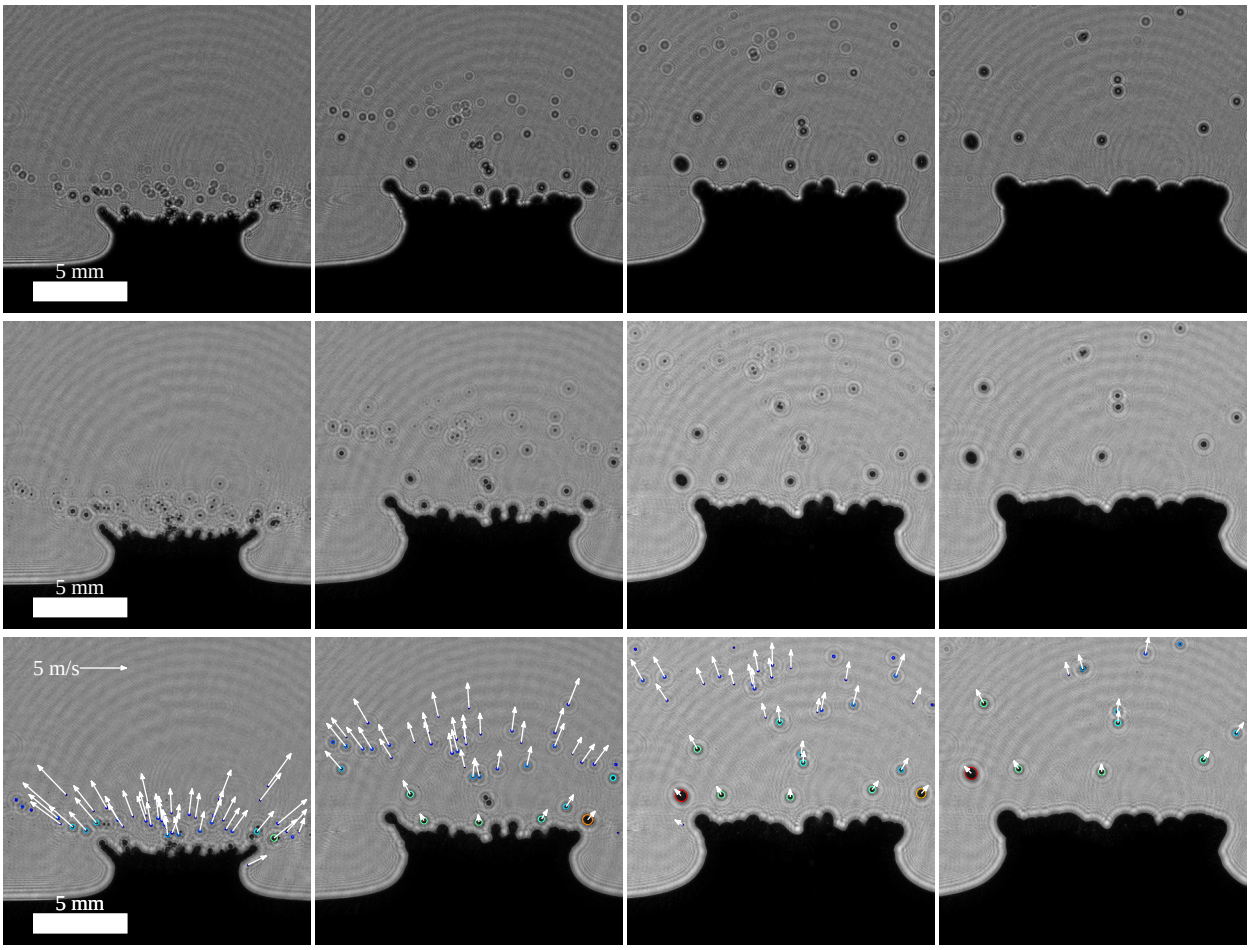

(a) τ = 2.5 (b) τ = 5.0 (c) τ = 7.5 (d) τ = 10.0

Figure 3. DIH results corresponding to the *We*=550 images shown in the second row of Figure 1: (top) recorded holograms, (middle) numerically refocused to the location of impact (z_0=105.9 mm), and (bottom) measured in-plane sizes and velocities.

In [13], up to 30 minutes were required to process a single hologram in a similar manner. In the current experiment, a typical DIH video of an impact event consists of roughly 600-700 frames. To enable data processing within a reasonable amount of time, significant efforts were undertaken to parallelize the processing routines and leverage graphical processing units (GPU) where possible. For the results presented here data were processed on a Dell Precision T7600 workstation equipped with dual Xeon E5-2665 cores operating at 2.4 GHz, 128 Gb of RAM, an NVIDIA K40 GPU and MATLAB v2014a with the parallel computing toolbox running 16 frames at a time. Data from approximately 12000 frames could be processed within a 24 hour period or equivalently a per frame processing time of about 7 seconds. Although significant differences in hologram sizes (4872×3248 pixels in previous work vs. 1024×1024 pixels in current work) contribute to the processing speedup, the results, nevertheless, represent an order-of-magnitude improvement in processing time.

Three component fragment velocities are determined by matching measured fragment positions in sequential frames. Because the measured x-y positions are expected to be significantly more accurate than the reconstructed z-position, we choose to match individual fragments from their x-y coordinates. Here, the match probability method (Hungarian routine) of Tinevez [19] is utilized. No match is accepted when the in-plane displacement is greater than 0.7 mm.

The third row in Figure 3 shows the measured in-plane velocities found in this manner. The results display the expected flow symmetry with few outliers. This indicates that the method has done a good job capturing in-plane velocities. However, the out-of-plane z-velocities show significantly higher uncertainty. For example, Figure 4 shows the measured velocities in the x-z plane at $\tau = 5$ (corresponding to the results shown in the second column in Figure 3). Clearly, many of the measured z-velocities are in error.

It is well known that DIH suffers from high uncertainty in the out-of-plane position caused by the depth of focus problem discussed in [2, 20]. Due to large pixel sizes and higher noise, one can expect this problem to be more significant for kHz CMOS sensors compared to low-speed CCDs. This appears to be confirmed by qualitative comparison of the results in Figure 4 to similar results presented in [13].

To quantify this uncertainty, Figure 5 shows a scatter plot of measured x and z-velocities from 26 different impact events at the conditions shown in Figure 3(b). Here, $\bar{x}$ and $\bar{z}$ are the mean position of all fragments measured at these conditions. Process symmetry dictates that the measured v_x and v_z should be statistically similar when plotted in this manner, and the much higher scatter in v_z is assumed to be due to measurement uncertainty. To quantify this, we assume that v_x has negligible uncertainty. The difference in the standard deviations of the measured x and z velocities with respect to the linear fits gives an estimate of the uncertainty in the z-velocity. Accounting for the interframe time, gives an estimated positional uncertainty of 1.5 mm. Finally, for comparison with other results in the literature, the uncertainty is normalized by the mean measured diameter at this condition ($\bar{d} = 162$ μm), resulting in an estimated z-positional uncertainty of $9.4 \cdot \bar{d}$.

In our previous work, the depth uncertainty of particles measured using low noise CCDs was estimated to be on the order of 1-2 particle diameters [13, 17, 18]. Although some of the variation in measurement uncertainty can likely be attributed to other differences in experimental methods and data reduction routines, these results clearly indicate that kHz DIH with current CMOS technology suffers from significant depth uncertainty.

Application of kHz DIH for quantitative measurements of 3D phenomena requires substantial improvement in this uncertainty. One possibility discussed in [12] is to use two orthogonal DIH systems to eliminate the depth uncertainty. Alternatively, here, we choose to use the knowledge that individual fragments must follow smooth trajectories over time and fit measured positions to these trajectories.

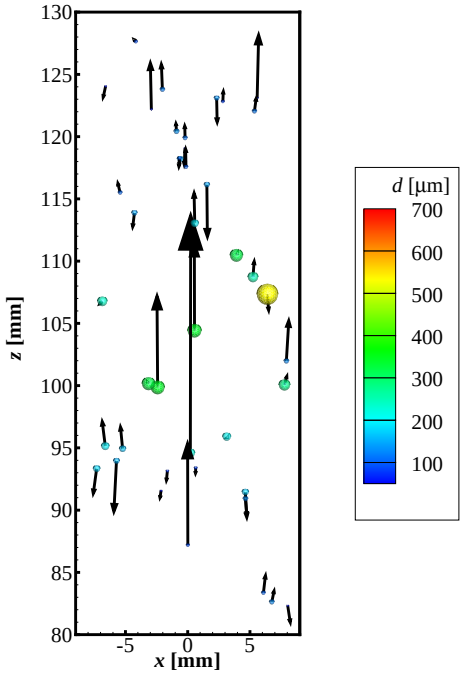

Figure 4. Out-of-plane velocities measured by frame-to-frame particle matching at We=550, τ=5 (second column in Figure 3).

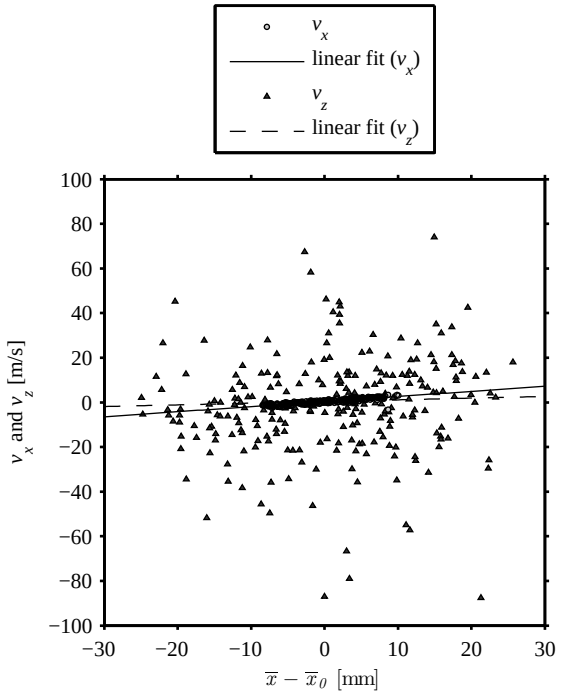

Figure 5. In-plane versus out-of-plane velocities measured by frame-to-frame particle matching. (1026 matches are measured and 250 are displayed).

Because the flow phenomena are relatively slow compared to the recording rate, individual fragments remain within the field of view of the DIH system in up to a few hundred frames. Consequently, the particle matching discussed previously can be extended to track single fragments though multiple frames. For example, Figure 6 shows the measured *x*-*y*-*z* positions over time for one fragment. As expected, the in-plane (*x*-*y*) positions show very little scatter, while the *z*-positions show significant scatter. Nevertheless, over a sufficiently long time-frame, the measured *z*-positions follow a clear trend.

To improve the accuracy of the temporal measurements, the *x*, *y*, and *z* positions are fit to simple models of their trajectories. Because *x* and *y* are well resolved, these trajectories are fit to a quadratic model with respect to time, while the *z*-trajectory is fit to a linear model. In Figure 6, the dotted line shows the best-fit trajectory in each direction. These are found using MATLAB®'s *fitlm*, linear regression fitting routine, with robust options which attempt to reduce the effects of outliers.

Figure 7 shows the resulting in-plane sizes and velocities after all trajectories have been fit in this manner. Here, trajectories are displayed which are a minimum of 30 frames in duration. Also, the fragment diameter is taken as the mean diameter along the trajectory. Careful comparison of Figure 7 with Figure 3 indicates that a few erroneous in-plane velocity vectors have been corrected with this method. More significantly, Figure 8 shows the velocities in the out-of-plane direction. Comparison with Figure 4 indicates that this method significantly improves the *z*-position and velocity measurements.

Finally, Figure 9 shows a comparison of the measured v_x and v_z. Compared with Figure 5, it is clear that the scatter in the *z*-velocity due to measurement uncertainty has been almost completely eliminated. Once again, the difference in standard deviations in v_x and v_z is used to derive an estimate of the *z*-positional uncertainty of $0.26 \cdot \overline{d}$.

These results demonstrate that, under appropriate conditions, kHz DIH can be used for quantitative measurement of 3D flows. In the next section, the method is applied to study temporal properties of the impact of a water drop on a thin film at multiple conditions.

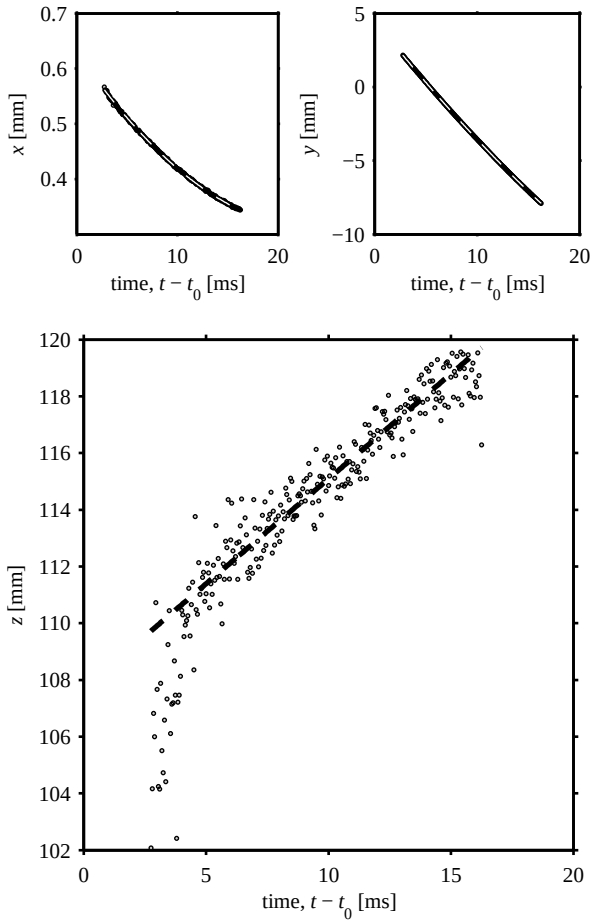

Figure 6. Measured *x* (top left), *y* (top right), and *z* (bottom) positions of a single fragment and the best-fit trajectories (dashed lines).

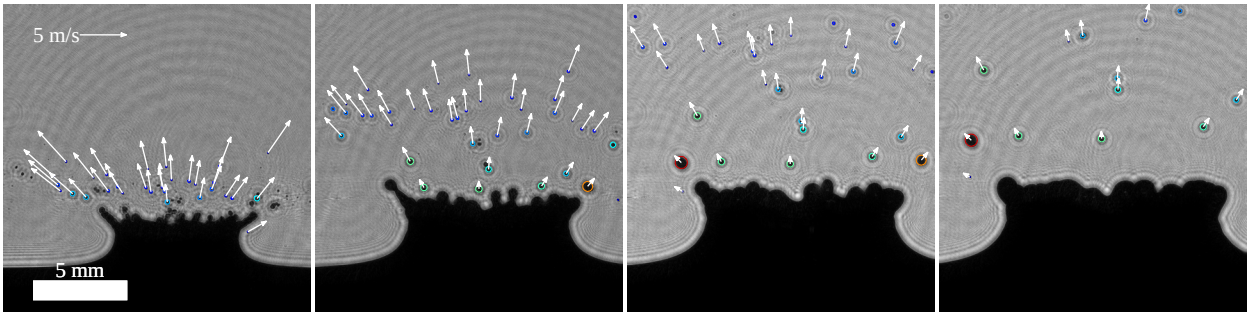

(a) τ = 2.5 (b) τ = 5.0 (c) τ = 7.5 (d) τ = 10.0

Figure 7. Measured in-plane sizes and velocities after fitting fragment tracks to smooth trajectories.

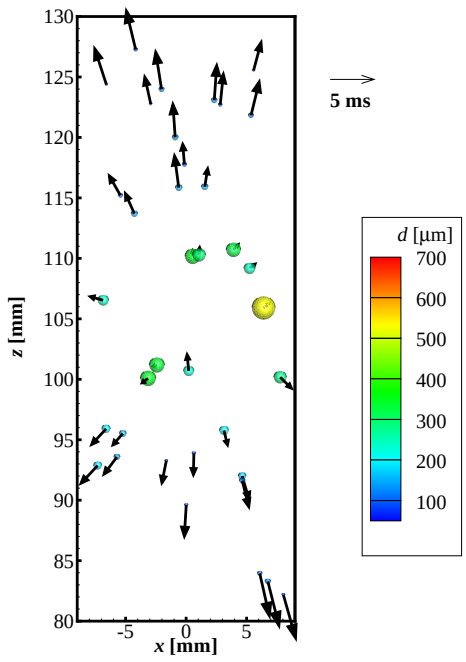

Figure 8. Out-of-plane velocities at *We*=550, τ=5 (second column in Figure 7) measured after fitting fragment tracks to smooth trajectories.

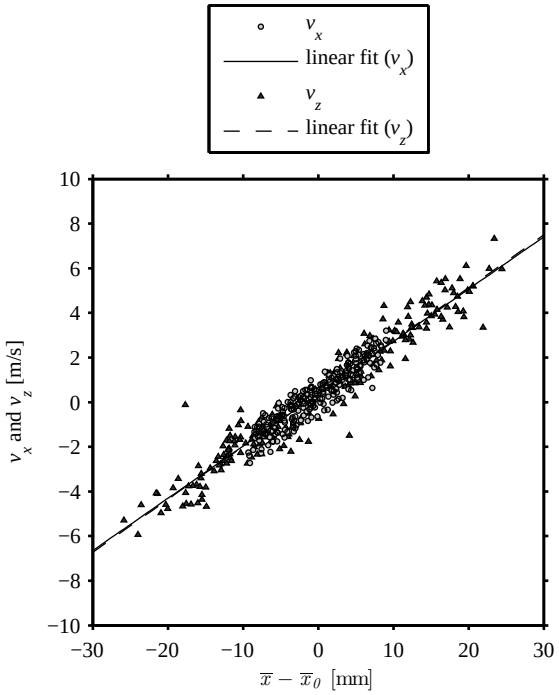

Figure 9. In-plane versus out-of-plane velocities after fitting fragment tracks to smooth trajectories (893 tracks are measured and 250 are displayed).

Experimental Results and Discussion

Table 1 summarizes the conditions studied here. Four separate *We* are investigated and at each condition approximately 20 DIH videos are analyzed. For each video, the methods described above are applied to quantify the trajectories of fragments. Additionally, the trajectory of the drop before impact is measured to find the initial drop diameter, d_0, impact time, t_0, impact velocity, v_0, and impact coordinates, x_0 and z_0.

Characteristic fragment sizes are presented as functions of *We* in Table 2. As reported by previous investigators [21, 22], increasing *We* leads to larger mean diameters (within experimental uncertainty) and increased spread in the size distributions.

Our previous investigation of drop impact relied on ensemble averaging to provide temporal statistics of all fragments within the field of view at a given time [13]. However, models [14, 23] predict behavior as a function of the time when fragments break off from the crown. Comparison of the results in [13] with such models is subject to the additional uncertainty and complexity needed to account for this averaging over the field of view. In contrast, kHz DIH enables individual fragments to be followed along their trajectories, such that the formation time can be estimated. Here is it assumed that the start time of a trajectory gives a good estimate of the time when the fragment pinches off from the crown, and in Figure 10 to Figure 13 temporal statistics are presented as functions of this time.

Table 1. Initial conditions, given as the mean from all videos ± the standard deviation of the mean from each video.

Approximate fall height (mm)	Number of videos analyzed	Initial diameter, d_0 (mm)	Impact velocity, v_0 (m/s)	Dimensionless film thickness, δ	Impact Weber number, *We*
600	22	2.639 ± 0.007	3.22 ± 0.01	1.124 ± 0.002	381 ± 2
900	26	2.619 ± 0.011	3.89 ± 0.01	1.115 ± 0.003	552 ± 5
1250	13	2.645 ± 0.009	4.48 ± 0.01	1.126 ± 0.003	737 ± 6
2250	20	2.648 ± 0.006	5.62 ± 0.02	1.127 ± 0.002	1160 ± 10

Table 2. Characteristic sizes of the fragments, given as the mean from all videos ± the standard deviation of the mean from each video.

Impact Weber number, *We*	Number of measured fragments	D_{10} (μm)	D_{30} (μm)	D_{32} (μm)
381 ± 2	59 ± 12	127 ± 19	159 ± 21	199 ± 36
552 ± 5	81 ± 11	137 ± 13	203 ± 19	298 ± 57
737 ± 6	74 ± 13	130 ± 18	192 ± 28	282 ± 48
1160 ± 10	99 ± 12	178 ± 18	260 ± 26	372 ± 49

The number of fragments produced is given as a function of non-dimensional time in Figure 10. Here, each symbol represents the mean number of fragments measured per video whose production time falls within $\tau \pm 0.25$. The corresponding uncertainty bars are the standard deviation of the mean from each video. As expected, the number of fragments initially increases as the impacting drop forms a crown, then a rim with fingers, and then fragments which separate from the fingers. The subsequent decrease is due to the cessation of finger formation as the rim begins to retract into the crown and the crown falls toward the free surface (see Figure 1). These results agree with previous ensemble average measurements which indicate that maximum fragment production occurs around $\tau \approx 2$ [13, 21].

Figure 10 also reveals some trends as a function of *We* which may not have been previously reported. Specifically, as *We* increases, (i) additional fragments are produced at $\tau \gtrsim 2$, (ii) the peak number of fragments is reduced, and (iii) the time at which the peak number of fragments is produced increases. As *We* increases, the velocity of the growing rim tends to increase, this likely results in greater momentum to sustain pinch off of fragments at later times.

Figure 11 illustrates how mean fragment size varies with time. The continual rise is expected due to deceleration of the crown and rim as the rim-to-film-surface distance increases. This deceleration leads to lower growth rates for finger formation and increases the size of fragments shed from them. In addition, these results are in reasonable agreement with the ½ power law suggested by theory [23].

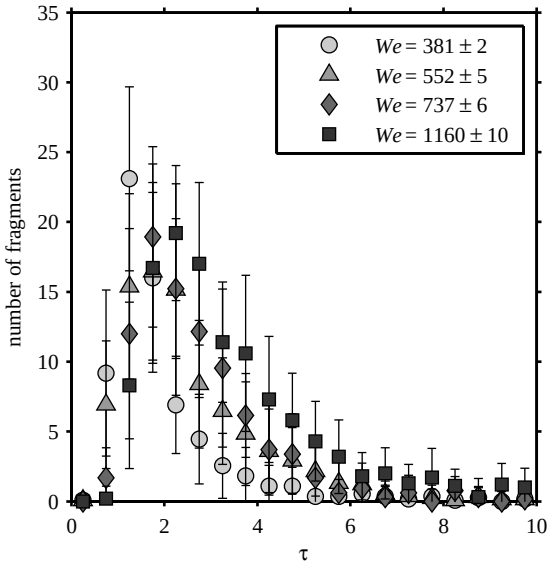

Figure 10. Mean number of fragments produced versus dimensionless time. Symbols are the means from all videos. Uncertainty bars are the standard deviation of the mean from each video.

Finally, Figure 12 and Figure 13 illustrate how fragment velocities evolve with dimensionless time. Figure 12 presents mean radial velocities, $\overline{v}_r$, in the *x*-*z* plane where the origin is taken as the location of drop impact (x_0, z_0). Figure 13 presents mean *y*-velocity, $\overline{v}_y$. As expected, both dimensionless velocity components decrease with dimensionless time. The $\overline{v}_r$ results in Figure 12 are consistent with those of Cossali *et al.* [21] and Yarin and Weis [23], who suggest exponent values near -½.

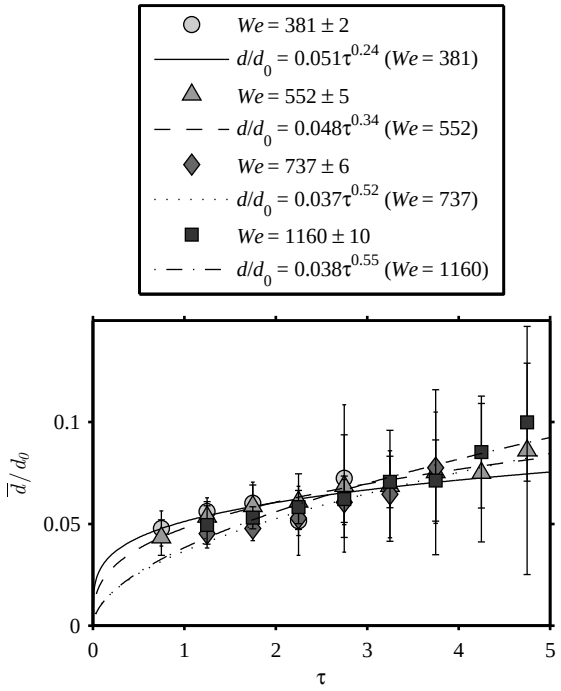

Figure 11. Dimensionless mean fragment size versus time. Symbols are the means from all videos. Uncertainty bars are the standard deviations of the mean from each video.

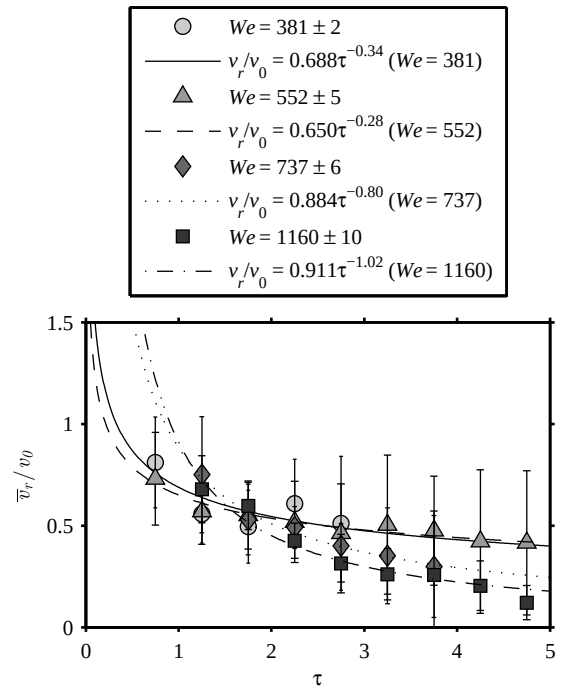

Figure 12. Dimensionless mean fragment radial velocity versus time. Symbols are the means from all videos. Uncertainty bars are the standard deviations of the mean from each video.

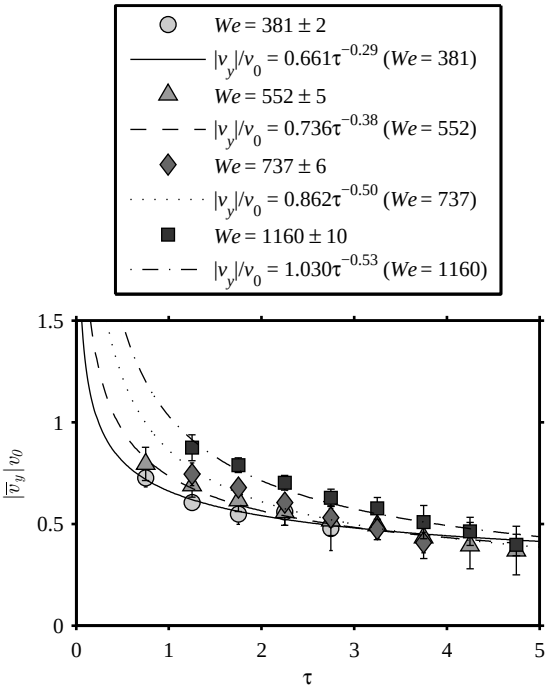

Figure 13. Dimensionless mean fragment *y*-velocity versus time. Symbols are the means from all videos. Uncertainty bars are the standard deviations of the mean from each video.

Summary and Conclusions

The work presented here demonstrates kHz digital in-line holography (DIH) and its use for 3D, temporal quantification of the fragments produced from the impact of a water drop on a thin film of water. High-speed CMOS sensors are shown to increase the depth uncertainty compared to low-speed CCD sensors. Nevertheless, by resolving fragment positions over multiple frames and fitting the trajectories to smooth models, excellent 3D positional accuracy is achieved.

Four Weber numbers from 381 to 1160 are investigated. Temporal resolution allows for quantification of fragment properties as a function of their formation time. The non-dimensional diameters are shown to increase as a function of time, while the non-dimensional velocities decrease over time.

Acknowledgements

This work was supported by the Weapons Systems Engineering Assessment Technology program, and the Laboratory Directed Research and Development program at Sandia National Laboratories which is a multiprogram laboratory operated by Sandia Corporation, a Lockheed Martin Company, for the United States Department of Energy's National Nuclear Security Administration under contract No. DE-AC04-94AL85000.

References

[1] Schnars, U., and Jueptner, W., *Digital holography: Digital hologram recording, numerical reconstruction, and related techniques*, Springer, 2005.

[2] Katz, J., and Sheng, J., *Annual Review of Fluid Mechanics*, 42: 531-555, (2010).

[3] Tian, L., Loomis, N., Domínguez-Caballero, J.A., and Barbastathis, G., *Applied Optics*, 49(9): 1549-1554, (2010).

[4] Lebrun, D., Allano, D., Méès, L., Walle, F., Corbin, F., Boucheron, R., and Fréchou, D., *Applied Optics*, 50(34): H1-H9, (2011).

[5] Gire, J., Denis, L., Fournier, C., Thiébaut, E., Soulez, F., and Ducottet, C., *Measurement Science and Technology*, 19(7): 074005, (2008).

[6] Gopalan, B., and Katz, J., *Physical Review Letters*, 104(5): 054501, (2010).

[7] Yang, Y., Li, G., Tang, L., and Huang, L., *Applied Optics*, 51(2): 255-267, (2012).

[8] Khanam, T., Nurur Rahman, M., Rajendran, A., Kariwala, V., and Asundi, A.K., *Chemical Engineering Science*, 66(12): 2699-2706, (2011).

[9] Spuler, S.M., and Fugal, J., *Applied Optics*, 50(10): 1405-1412, (2011).

[10] Wu, Y., Wu, X., Wang, Z., Chen, L., and Cen, K., *Applied Optics*, 50(34): H22-H29, (2011).

[11] Seifi, M., Fournier, C., Grosjean, N., Méès, L., Marié, J.-L., and Denis, L., *Optics Express*, 21(23): 27964-27980, (2013).

[12] Buchmann, N.A., Atkinson, C., and Soria, J., *Measurement Science and Technology*, 24(2): 024005, (2013).

[13] Guildenbecher, D.R., Engvall, L., Gao, J., Grasser, T.W., Reu, P.L., and Chen, J., *Experiments in Fluids*, 55: 1670, (2014).

[14] Yarin, A.L., *Annual Review of Fluid Mechanics*, 38(1): 159-192, (2006).

[15] Moreira, A.L.N., Moita, A.S., and Panão, M.R., *Progress in Energy and Combustion Science*, 36(5): 554-580, (2010).

[16] Gao, J., Guildenbecher, D.R., Engvall, L., Reu, P.L., and Chen, J., *Applied Optics*, 53(27): G130-G138, (2014).

[17] Guildenbecher, D.R., Gao, J., Reu, P.L., and Chen, J., *Applied Optics*, 52(16): 3790-3801, (2013).

[18] Gao, J., Guildenbecher, D.R., Reu, P.L., and Chen, J., *Optics Express*, 21(22): 26432-26449, (2013).

[19] Tinevez, J.-Y., "Simple tracker," http://www.mathworks.com/matlabcentral/fileexchange/34040-simple-tracker, 2012.

[20] Meng, H., Pan, G., Pu, Y., and Woodward, S.H., *Measurement Science and Technology*, 15(4): 673, (2004).

[21] Cossali, G.E., Marengo, M., Coghe, A., and Zhdanov, S., *Experiments in Fluids*, 36(6): 888-900, (2004).

[22] Okawa, T., Shiraishi, T., and Mori, T., *Experiments in Fluids*, 41(6): 965-974, (2006).

[23] Yarin, A.L., and Weiss, D.A., *Journal of Fluid Mechanics*, 283: 141-173, (1995).